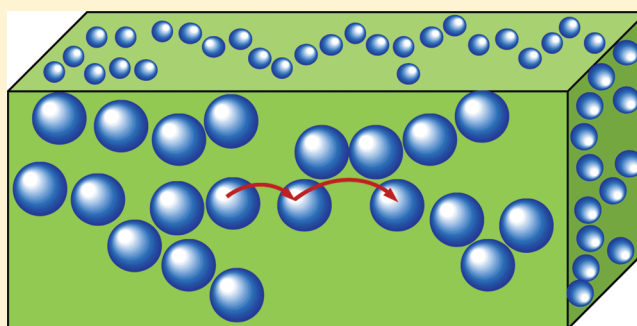# Investigation of Nanostructure in Room Temperature Ionic Liquids using Electronic Excitation Transfer

Kendall Fruchey, Christian M. Lawler, and M. D. Fayer*

Department of Chemistry, Stanford University, Stanford, California 94305, United States

S *Supporting Information*

ABSTRACT: Donor–donor electronic excitation transfer among 9-phenylanthracene (9PA) chromophores was measured in the room temperature ionic liquid (RTIL) 1-methyl-3-octylimidazolium chloride using time dependent fluorescence depolarization. 9PA, which is uncharged and nonpolar, will partition into the organic regions of the RTIL. The excitation transfer rate, which is sensitive to the distribution of chromophores in the RTIL, is modeled using different spatial configurations of 9PA molecules in the RTIL solution. The models are an isotropic distribution (random distribution) and a clustered sphere model to represent hydrophobic regions of a nanostructured environment. Model calculations were performed to demonstrate the sensitivity of excitation transfer to different distributions of chromophores. When compared to the experiment, the isotropic model can adequately match the data. From a Bayesian analysis of the sensitivity of the excitation transfer to the models for the spatial distribution of chromophores, an upper limit of 6 Å radius is placed on the size of hydrophobic domains in the RTIL.

I. INTRODUCTION

The concept of nanostructuring in room temperature ionic liquids (RTILs) has been an important issue in understanding the properties of RTILs. In addition to fundamental interest, possible RTIL nanostructuring has been invoked to explain phenomena in their applications, such as gas sequestration,[1] photochemistry,[2] solar devices,[3] and electrodeposition.[4] Spatial heterogeneity, or nanostructuring, in RTILs has been difficult to quantify. Nanostructuring is roughly defined as an aggregation of the long alkyl chains due to a combination of electrostatics and the hydrophobic effect. The structure has also been likened to that of a bicontinuous emulsion on a much smaller scale.[4] The effect was first noted in computer simulations, most notably those of Wang and Voth[5] and Canongia-Lopes and Pádua.[6] While some effort to quantify the properties of the nanostructure organization were undertaken based on these simulations, especially with the development of a heterogeneity order parameter,[7] there is substantial ambiguity on what nanostructuring means. In some sense, the strongest understanding came from the color coded snapshots from simulation trajectories that, while visually striking, do not fully quantify the phenomenon.

Experimental indications of spatial heterogeneity have come from a variety of sources,[8,9] particularly X-ray scattering experiments.[10–14] The connection between these studies and what is typically understood when discussing the nanostructuring has, however, been called into question by neutron studies which do not indicate the presence of substantial nanostructuring.[15] The neutron scattering experiments and other

work[16] has contracted the length scale over which the nanostructured hydrophobic regions likely exist. However, very recent experimental work again advances the idea of mesoscopic segregation.[17,18] The length scale of the nanostructuring is still an outstanding question. Size estimates have varied widely from tens of nanometers[9] to 18 Å[19] to 6–8 Å.[20]

One consequence of the amphiphilic nature of the ionic liquid is the selective solvation of molecules dissolved in the RTIL. In the context of a nanostructured solvent, this is equated with partitioning of the solute into the appropriate phase. Evidence for this phenomenon has be seen in fluorescence[21,22] and optical Kerr effect studies.[23] This partitioning appears to preserve the features of the surrounding solvent, such that the intruding probe molecules do not substantially perturb the surrounding solvent structure. For an ionic liquid, in which minimizing the strong Coulomb interactions between ions is likely the dominant force, this is not surprising. Thus, the distribution of an appropriately chosen probe can report on the structure of the region into which it partitions because of favorable interactions.[21]

Excitation transfer has been successfully used as a tool to address the structural nature of a variety of systems.[24–27] Frequently, the method involves experiments with a single excitation transfer step between a donor and an acceptor.[28,29] The single donor/acceptor transfer experiment is used to gain

some information about two positions, e.g. on a protein. For systems in which information on a more global spatial configuration is desired, either dilute donors with many acceptors or donor−donor excitation transfer can be used.[24−27] At its heart, the use of excitation transport to determine spatial distribution is based on the high spatial sensitivity of the Förster excitation transfer mechanism. The rate of excitation transfer has a $1/r^6$ dependence where r is the separation between chromophores. For a single donor and a single acceptor, r is the separation between the chromophores. The sensitivity to the spatial distribution is retained for chromophore systems with many donors and acceptors that can participate in the transfer dynamics. However, the mathematical treatment of the problem becomes more intense. Donor−donor transfer is preferable to donor−acceptor transfer in many situations because only a single type of chromophore is needed. Employing a single type of chromophore avoids the possibility that the two types of chromophores are not distributed identically in a spatially heterogeneous system.

The presence of many donors in a donor−donor excitation transfer system creates numerous pathways for the excitation to migrate. A detailed and accurate solution to the donor−donor excitation transfer problem for molecules randomly distributed in solution was provided by Gochanour, Andersen, and Fayer (GAF).[30] Using a topological reduction, the GAF theory provides a solution to the problem of energy migration that incorporates an infinite number of particles and pathways. The theoretical results were related to the experimental observable of excitation transport induced fluorescence depolarization, and excellent agreement was found between theory and experiments for molecules randomly distributed in solution.[31] However, the GAF theory is not applicable to heterogeneous systems because it requires translational invariance of the ensemble averaged Green's function solution to the equations. Other methods have been used for restricted and other complex geometries.[25,27,32−34]

An approach developed by Huber for isotropic liquids,[35,36] which is based on a two-body approximation, was shown to give results essentially identical to the GAF self-part of the Greens function.[37] It is the self-part of the Greens function that is directly related to the fluorescence depolarization observable. The Huber theory for isotropic solution was extended to treat spatially heterogeneous and finite volume systems, especially polymers[24,38−40] and micelles.[41,42] The experiments demonstrated that quantitative information on the spatial distribution of chromophores can be obtained from fluorescence depolarization experiments and the appropriate application of theory.

Of particular interest here is the theory of clustered chromophore systems,[43] which is capable of being extended to treat an inhomogeneous solvent similar to the structure postulated to exist in the RTILs. Prior studies have shown that nonpolar solutes are selectively solvated by the nonpolar tails of RTILs.[21] In the context of a nanostructured RTILs, nonpolar chromophores will segregate into the nonpolar domains. The segregation into nonpolar domains will result in a nonrandom distribution of chromophore positions throughout the liquid, which in turn will be manifested by modifying the electronic excitation pathways available to a concentrated system of chromophores relative to chromophores randomly distributed in solution.

In this study, the nonpolar chromophore 9-phenylanthracene (9PA) was used to study the process of excitation transfer in a highly viscous ionic liquid 1-methyl-3-octylimidazolium

chloride (OmimCl). The structures are shown in Figure 1. 9PA was chosen to be relatively small in size, nonpolar, soluble in
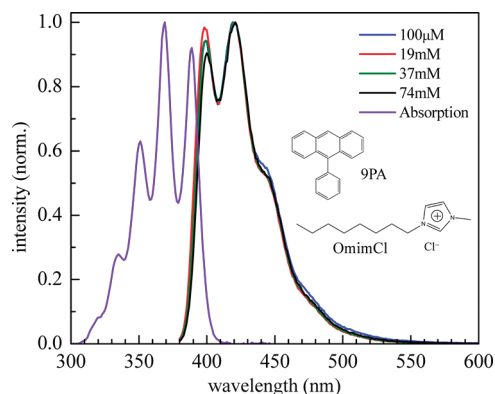

Figure 1. Normalized fluorescence and absorption spectra for the 9PA dissolved in OmimCl. The molecular structures are shown in the figure. The different fluorescence curves correspond to the different 9PA concentrations used in the study. At all concentrations the absorption spectra were essentially identical.

relatively large concentrations without forming dimers, and to have a donor−donor Förster radius on the order of the expected spatial heterogeneity. OmimCl was chosen because prior experiments indicate it is potentially nanostructured, and because high viscosity is required to separate the effect of molecular rotation from the excitation transfer. The nanostructuring corresponds to a restricted spatial distribution of the 9PA, which is partitioned into nonpolar domains. Experimental evidence that 9PA partitions into the alkyl regions of OmimCl is given in the Supporting Information. Previous studies also support the selective partitioning of molecules like 9PA into the hydrophobic regions of RTILs.[21,44] The deviation from the isotropic distribution of chromophores, which occurs in normal solvents, will have a direct effect on the excitation transfer process, and therefore, on the fluorescence depolarization time dependent observable. Using a clustered chromophore excitation transport model, it is possible to obtain the length scale on which heterogeneity exists.

II. EXCITATION TRANSFER THEORY

The basis for this work is an extension of the original Huber theory[35,36] to consider clustered systems.[37,43] The quantity of interest throughout is $\langle G_s(t) \rangle$, which denotes the probability that an excitation resides on the originally excited molecule at time t. $\langle G_s(t) \rangle$ has contributions from excitations that have not left the initially excited chromophore and from excitations that have transferred to other chromophores and then returned to the initially excited chromophore. The fluorescence polarization decays as $\langle G_s(t) \rangle$ decays.[31] The rate at which the excitation is lost from the originally excited molecule depends on the spatial configuration of other chromophores and also on the Förster dipole−dipole coupling transfer rate.[45] The single pair of chromophores rate is

$$E(t) = \frac{1}{2}\left[1 + \exp\left(-\frac{2t}{\tau}\left(\frac{R_0}{r}\right)^6\right)\right]$$

(1)

$\langle G_s(t) \rangle$ can be described for any spatial distribution of chromophores using[37]

$$\ln \langle G_s(t) \rangle = \frac{-c}{2} \int_0^\infty \left[1 - \exp\left(\frac{-2t}{\tau} \left(\frac{R_0}{|\mathbf{r}|} \right)^6 \right) \right] u(\mathbf{r}) \, d\mathbf{r}$$

(2)

where c is the concentration of chromophores, τ is the fluorescence lifetime, and R_0 is the Forster radius. $u(\mathbf{r})$ is the vector distribution defined so that $cu(\mathbf{r}) \, d\mathbf{r}$ is the probability of finding another chromophore at $\mathbf{r}$ relative to the initially excited molecule, which is set at the origin. For an isotropic system in which all initial positions are equivalent, eq 2 can be directly evaluated analytically yielding

$$\langle G_s(t) \rangle = \exp\left[\frac{-(8\pi^3)^{1/2}}{3} cR_0(t/\tau)^{1/2} \right]$$

(3)

This relation has been experimentally verified in a number of randomly distributed systems[31,39] and also compares very well with the more detailed GAF theory for times $(t < 2\tau)$ and reduced concentrations $C = (4\pi/3)cR_0^3 < 2$.[37] For chromophores on nonidentical sites, an average over configurations must be performed on eq 2, yielding

$$\langle G_s(t, N) \rangle = 1/V_d \int_{V_d} G_s^1(t, \mathbf{r}_d) u(\mathbf{r}_d) \, d\mathbf{r}_d$$

(4a)

$$G_s^1(t, \mathbf{r}_d, N)$$
$$= \exp\left[-\frac{(N-1)}{2V_a} \int_{V_a} \left\{ 1 - \exp\left(-\frac{2t}{\tau} \left(\frac{R_0}{r_{ad}} \right)^6 \right) \right\} * u(\mathbf{r}_a) \, d\mathbf{r}_a \right]$$

(4b)

where $u(\mathbf{r}_j)$ is the distribution of chromophores. Here all of the chromophores are the same type of molecule since the experiments measure donor–donor transfer. For the notation, we will call the initially excited chromophore the donor (d) and all other identical chromophores the acceptors (a). V_j is the volume of the region of space occupied by the donor (d) and the acceptors (a); N is the total number of chromophores (donor + acceptors), and r_{ad} is the distance between the donor and an acceptor. Equation 4 is the basis for all subsequent calculations, which involve incorporating the appropriate forms of $u(\mathbf{r})$, the spatial distribution of the chromophores.

A particular form of $u(\mathbf{r})$ must be supplied that models the chromophore distribution. Then, a comparison between the calculations and the experimental data results in a test of the model. To describe the possible nanostructuring of RTILs in a form that reflects the important characteristics of the nanostructuring while remaining computationally tractable, a system of clustered spheres is used. The 9PA will partition into the hydrophobic regions. These hydrophobic regions are treated as spherical cavities of radius R_s, and a hard sphere radial distribution function is employed. This model incorporates the important feature of nanostructuring with the hydrophobic regions as populated cavities and excluded exterior spaces as the hydrophilic regions of cationic head groups and anions. The chromophores can be distributed anywhere within the hydrophobic pockets, that is they are locally isotropic.

Marcus et al. give a complete treatment of excitation transport in clustered systems.[43] An important result is that $\langle G_s(t) \rangle$ can be factored into two parts,

$$\langle G_s(t) \rangle = \langle G_s^{on}(t) \rangle \langle G_s^{off}(t) \rangle$$

(5)

corresponding to the probability decay as the result of excitation transfer within the cluster (on), and excitation transfer between clusters (off). Breaking up the calculation simplifies the expressions. Each part is treated separately.

$\langle G_s^{on}(t) \rangle$ can be obtained by applying the appropriate spherical geometry to eq 4. A change of coordinates simplifies the calculations.[37] The interior integration is performed over the vector separating the donor and acceptor, $\mathbf{r}_{ad}$. The exterior integration is over all $\mathbf{r}_d$ relative to the sphere's center, but $\mathbf{r}_a$ is recast as a function of spherical coordinates of r_{ad} and θ_{ad}, where θ_{ad} is the angle between the $\mathbf{r}_d$ and $\mathbf{r}_a$. Using this transformation, eq 4 becomes

$$\langle G_s^{on}(t, N) \rangle = \frac{4\pi}{V} \int_0^{R_s} r_d^2 \left\{ \exp\left[\frac{-\pi(N-1)}{V} \int_{-1}^1 dq \right. \right.$$
$$\left. \left. \times \int_0^{f(r_d, q)} \left(1 - \exp\left[\frac{-2t}{\tau} \left(\frac{R_0}{r_{ad}} \right)^6 \right] \right) r_{ad}^2 \, dr_{ad} \right] \right\} dr_d$$

(6)

where $q = \cos(\theta_{ad})$, and $f(q, r_d) = (R_s^2 + r_d^2 - 2r_d^2(1 - q^2) - 2qr_d(R_s^2 - r_d^2(1 - q^2))^{1/2})^{1/2}$.

The tendency of the curves for $\langle G_s^{on}(t) \rangle$ to be unity at small R_s is the result of a constant chromophores density, which makes the population of individual spheres scale with R_s^3. This result has been compared to a more exact treatment, and it has been found to agree well when the two-body approximation is applicable $(t < 2\tau$ and $c < 2)$.[32,46]

$\langle G_s^{off}(t) \rangle$ is obtained in a similar fashion from eq 4, except that the integration for the donor and acceptor molecules are over different spheres separated by distance D. The problem is first treated with a single fixed D and then expanded to consider a large number of spheres at different separations. To compactly perform the required integrations, a multiframe coordinate system is used.[43] The transformation of $\mathbf{r}_a \to \mathbf{A}\mathbf{r}_{ad}$ changes eq 4 into

$$\langle G_s^{off}(t, D, N) \rangle = \frac{2\pi}{V_d} \int_0^{R_s} \int_0^\pi G_s^1(r_d, t, N, D) \sin(\theta) r_d^2 \, dr_d \, d\theta_d$$

(7)

$$G_s^1(r_d, t, N, D)$$
$$= \exp\left[\frac{N-1}{\pi V_a} \int_0^{R_s} \int_0^\pi \left(\exp\left[\frac{-2t}{\tau} \left(\frac{R_0}{r_{ad}} \right)^6 \right] - 1 \right) r_a^2 \sin(\theta_a) \, dr_a \, d\theta_a \right]$$

$$|r_{ad}|^6 = [r_d^2 + r_a^2 + 2D[r_a \cos(\theta_a) - r_d \cos(\theta_d)] - 2r_a r_d \cos(\theta_a - \theta_d) + D^2]^3$$

The limit of $D = 0$ gives the case of two spheres sitting on top of one another, which yields another route to $\langle G_s^{on}(t, N) \rangle$. For all other cases, eq 7 must be treated numerically.

To have a detailed model of the ionic liquid structure, the result of integrating eq 7 must be expanded to consider a large number of spheres at different spacings. The decay of $\langle G_s^{off}(t, D, N) \rangle$ can be written as a product of all pairwise interactions between spheres. Taking the limit as the number of

spheres becomes large leads to the thermodynamic limit of $\langle G_s^{off}(t,N)\rangle$, which can be expressed as[43]

$$\langle G_s^{off}(t, N)\rangle = \exp[-4\pi c_s \int_{2R_s}^{\infty}[1 - G_s^{off}(t, D, N)]g(D)D^2 \, dD]$$

(8)

for a distribution of spheres of macroscopic concentration c_s and radial distribution $g(D)$. The radial distribution function reflects the possible structures of the RTIL. The lower bound is set to prevent overlap of spheres, and the upper limit is expanded to infinity because the contribution from spheres outside several R_0 is negligible.

At this point, $\langle G_s(t,N)\rangle$ has been solved for a constant number (N) of chromophores per cluster. Since only the macroscopic cluster concentration will be specified, the distribution in chromophore number must be treated. Assuming the chromophores do not interact, the number of chromophores in any sphere will follow a Poisson distribution. Therefore, the observed $\langle G_s(t,c)\rangle$ is the product of Poisson weighted contributions of $\langle G_s^{on}(t,N)\rangle$ and $\langle G_s^{off}(t,N)\rangle$, with eq 6 becoming

$$\langle G_s^{on}(t, c)\rangle = \sum_{N=1}^{\infty}\left(\frac{e^{-\nu}\nu^{N-1}}{(N-1)!}\right)\frac{4\pi}{V}\int_0^{R_s}r_d^2\exp\left[\frac{-\pi(N-1)}{V}\right.$$

$$\times \int_{-1}^{1}dq\int_0^{f(r_d,q)}\left(1 - \exp\left[\frac{-2t}{\tau}\left(\frac{R_0}{r_{ad}}\right)^6\right]\right)r_{ad}^2 \, dr_{ad}\right]$$

(9)

and eq 7 becoming

$$\langle G_s^{off}(t, c)\rangle = \exp\left[-4\pi c_s\sum_{N=1}^{\infty}\left(\frac{e^{-\nu}\nu^{N-1}}{(N-1)!}\right)\right.$$

$$\times \int_{2R_s}^{\infty}[1 - G_s^{off}(t, D, N)]g(D)D^2 \, dD\right]$$

(10)

ν is the expectation number of chromophores in a sphere, which is equal to the macroscopic concentration of chromophores divided by the concentration of spheres. This form of the Poisson distribution neglects all contributions from clusters containing $N = 0$, because they will not contribute to fluorescence events.

Combining eqs 9 and 10 in eq 5 gives the final result for the $\langle G_s(t,c)\rangle$. The importance in this quantity lies with its connection to experimental observables. For a randomly oriented distribution of chromophores, polarized fluorescence comes from the initially excited molecule.[47] Therefore, the decay of the polarization of the fluorescence reports on the probability that the emission comes from the same molecule that was initially excited, $\langle G_s(t,c)\rangle$.

If the molecular rotation is slow and uncorrelated with the excitation transfer, then the anisotropy, defined as

$$r(t) = \frac{I_{\parallel}(t) - I_{\perp}(t)}{I_{\parallel}(t) + 2I_{\perp}(t)}$$

(11)

can be represented as the product of the anisotropy decay due to molecular rotation, and the anisotropy decay due to excitation transfer,[43]

$$r(t) = \Theta(t)\langle G_s(t, c)\rangle$$

(12)

The contribution from molecular rotation, $\Theta(t)$, can be measured in a low concentration sample in which excitation transfer is absent. Because the chromophores in this experiment are very slowly rotating, the frequently used orientationally averaged Forster rate is not applicable. The experimental situation considered here can be calculated from the orientational relaxation rate and the expected excitation transfer rate through a correction factor included in the Forster transfer rate.[48] The correction applies to the orientational factor $\langle \kappa^2\rangle$ in the Forster coupling to reflect the amount of orientational averaging experienced while undergoing excitation transport. For these experiments, $\tau_{rot} \simeq 5\tau_{transfer}$, for which the correction is between 0.84 and 0.90, depending on chromophores concentration. Thus, each instance of the Forster rate incorporates this concentration dependent factor $\Gamma(c)$, as

$$\left(1 - \exp\left[-\frac{2t}{\tau}\Gamma(c)\left(\frac{R_0}{r_{ad}}\right)^6\right]\right)$$

(13)

III. EXPERIMENTAL PROCEDURES

1-Methyl-3-octylimidazolium chloride (OmimCl) was obtained from Iolitec at 99+% purity. 9-Phenylanthracene (9PA) was obtained from Aldrich at maximum purity and used without further purification. The OmimCl was dried under vacuum at 60 °C for 5 days and then transferred into a nitrogen glovebox. Water content was measured using Karl Fischer titration (Mettler DL39) to be less than 500 ppm by weight. A carefully prepared stock solution of 9PA in methylene chloride was made using calibrated glassware. Measured amounts of this stock solution were added to a test tube and the solvent gently evaporated, leaving behind the 9PA. These dried tubes were transferred to the glovebox and then stirred with precisely weighed quantities of dry OmimCl. The ionic liquid solution was then transferred to a custom sample cell with variable path length and sealed in a constant temperature cryostat (Janus ST-100) under dry nitrogen. Absolute exclusion of additional water was imperative, as small quantities of absorbed water will change the viscosity of the sample, making correction for the solute rotation unreliable. Samples were prepared with peak optical densities of ~0.3 to minimize fluorescence absorption and re-emission. This was accommodated by using the variable path length to ensure the different concentration solutions satisfied the 0.3 maximum absorbance. The absorption in the region of overlap of the absorption and emission was far less.

The experimental setup for the time correlated single photon counting system has been described previously.[21] The system has an approximately Gaussian instrument response function of 28 ps fwhm. Since the relevant fluorescence and anisotropy decay times in this study were significantly greater than the instrument response time, deconvolution was not necessary to achieve accurate results. Samples were excited at 375 nm, and after passing through a long pass Schott glass filter to remove scattered excitation light, the fluorescence was resolved with a monochromator and detected at 426 nm with a channel plate detector. For each sample, time dependent fluorescence intensities were collected in parallel, perpendicular, and magic angle (54.7°) geometries. For the low concentration sample, the excitation volume in the cuvette was moved around to minimize the impact of photobleaching, which could interfere with proper removal of background fluorescence. For all high concentration samples, the effect of background fluorescence

was negligible. For the low concentration sample, the background fluorescence of trace impurities in the OmimCl was removed by swapping in a blank sample and then performing the experiment under identical conditions.

On each sample, a UV/vis absorption spectrum was taken with a Cary 6000i spectrometer. Steady state fluorescence scans were taken with 375 nm excitation wavelength on a Fluorolog 3 fluorimeter. No evidence for excimers or dimers was seen in the fluorescence spectra for the concentrations used as shown in Figure 1.

The Förster radius R_0 of 9PA was also calculated as 19.7 ± 0.7 Å from the measured overlap integral, quantum yield, and using literature values for index of refraction.[49] Extinction coefficients were measured from dilutions of calibrated ionic liquid solutions. The background subtracted absorption spectra were measured on the Cary 6000i spectrometer at 1 mm path length. The fluorescence quantum yield was measured using the comparison method with 9,10-diphenylanthracene as the standard.[50] For the ionic liquid samples, stock 9PA solutions were diluted to absorbances between 0.01 and 0.1 at 1 cm path length. The samples were stirred and warmed to 50 °C overnight to remove bubbles. The preparations were done entirely in the glovebox and, therefore, oxygen free. 9,10-Diphenylanthracene solutions were made from dilutions of stock solutions to a similar absorbance range in cyclohexane. Prior to sealing in cuvettes, the solutions were deoxygenated by bubbling cyclohexane saturated nitrogen through the solution for 15 min. The fluorescence measurement was performed on the Fluorolog-3 fluorimeter. The fluorimeter was warmed up and set at 375 nm excitation wavelength for all samples, performed in randomized order without changing any fluorimeter parameters. Because the ionic liquid has a very high viscosity and cyclohexane has a low viscosity, orientational relaxation is small in the ionic liquid over the fluorescence lifetime while it is complete in cyclohexane. To make the steady state fluorescence measurements in the two liquids independent of orientational relaxation and therefore comparable, polarizers were used at the magic angle to remove rotational effects. Additionally, a Schott glass absorber was placed on the emission side to completely remove any scattered light. In a randomized order, each sample's fluorescence was measured and then immediately placed in the Cary 6000i to measure absorption relative to the appropriate solvent blank. Auto-fluorescence was subtracted in the ionic liquid samples from an identically treated blank. The measurements gave a fluorescence quantum yield of 0.14 ± 0.03. In the time-resolved experiments, the fluorescence lifetime of the 9PA was single exponential with a decay time of 7.18 ns.

IV. RESULTS

A. Model Calculations. In performing calculations using eq 10, a bulk cluster concentration (sphere concentration) is required. For polymers or micelles, the cluster concentration is straightforward; it is the bulk concentration of polymer or micelles. To investigate the possible spatial heterogeneity in the RTILs, a different approach must be taken. The concentration of spheres is obtained by assuming a bulk volume fraction of spheres φ.

$$c_{cluster} = \frac{3\phi}{4\pi}\left(\frac{R_0}{R_s}\right)^3 \tag{14}$$

Similarly, the expectation value for the chromophore number per sphere is given by

$$\nu = \frac{CR_s{}^3}{\phi} \tag{15}$$

where C is the reduced chromophore concentration (see expression above eq 4). For the case of OmimCl, the volume fraction was estimated using the van der Waals volumes of the ions. The hydrophobic regions were assumed to be composed of some collection of the eight carbons on the octyl chain. The hydrophilic regions were taken to be a collection of the methylimidazolium part of the cation, and the entirety of the chloride anion. Using these divisions, a volume fraction of 0.7 is calculated. At low occupation numbers ν, the time dependent contributions to the fluorescence depolarization come from the $N = 2$ term in the Poisson average. In this limit, the factors of φ in the cluster concentration and chromophore expectation number in eq 10 multiply and cancel.

Using eqs 9 and 10, it is possible to model $\langle G_s(t)\rangle$ curves for different spatial distributions. Numerical integrations were performed using iterated Legendre−Gauss quadrature. Figure 2 shows some predicted curves for a reduced bulk chromophores concentration of $C = 1.5$ using clustered spheres and the isotropic model. For these model calculations, the radial distribution function for the spheres in eq 10 was made isotropic, i.e. $g(D) = 1$ for $D > R_s$. The choice of radial distribution function is discussed later in the section.
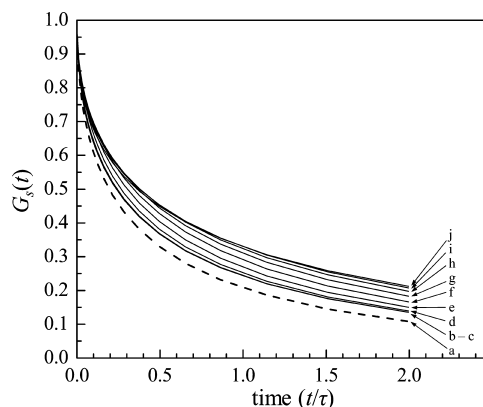

Figure 2. $\langle G_s(t)\rangle$ calculated from the clustered sphere model for various normalized R_s (the sphere radius divided by the Förster transfer radius R_0) and also for the isotropic model. The isotropic model curve is a. Curves for clustered spheres of R_s = 0.1, 0.2, 0.3, 0.4, 0.5, 0.6, 0.7, 0.8, and 0.9 are labeled b−j sequentially. The curves for b and c are on top one another. The time coordinate is normalized relative to the fluorescence lifetime for this and all subsequent plots.

For very small sphere radii, the curves predicted by the clustered sphere model approach the isotropic model. The similarity comes from the short distances over which the distribution of the chromophores changes relative to R_0, which averages out any structure. In effect, the clusters themselves act like individual chromophores. Since the spheres are almost isotropically distributed, the effective chromophores distribution also looks isotropic. There is a small difference between the small sphere limit and isotropic model because of the quantization in the Poisson average used for the sphere calculation. The functional form of the curve is the same as the case of the isotropic model, but the effective reduced

3058

dx.doi.org/10.1021/jp207757r | J. Phys. Chem. B 2012, 116, 3054−3064

concentration is decreased by about 5%. In an experiment, these curves will be indistinguishable within the experimental error in measuring the Förster radius.

The other limiting case is at very large sphere radius. The model again begins to look isotropic because the majority of the chromophores are too far removed from the boundary of the sphere to feel its effect. Since the chromophores inside the spheres are isotropically distributed, this recovers the bulk isotropic curve shape. Again the concentration is scaled, but this time by the inverse volume fraction. The excitation transfer in this limit is dominated by the $\langle G_s^{on}(t) \rangle$. But within the sphere, the effective chromophores concentration is enhanced relative to the apparent bulk concentration by the volume fraction, increasing the rate of excitation transfer. Between these two extremes, the clustered sphere model shows a difference from the isotropic model that is very sensitive to the size of spheres.

The region of sensitivity of the excitation transfer to sphere size, and therefore, the size of nanostructured domains, is for sphere radii from approximately $0.3R_0$ to $3R_0$. The range of sensitivity depends slightly on the average chromophore number per sphere. As the size of the sphere is increased at constant bulk concentration and volume fraction, the rate of excitation transfer initially decreases as the excluded regions between spheres become important. The trend continues until about $R_s = 0.8R_0$, when the excitation transfer reaches its slowest rate. Further increasing the size of the sphere will then begin increasing the rate of excitation transfer, particularly at early time. The time coordinate of $\langle G_s(t) \rangle$ is in some sense a measure of distance. The transfer rate in eq 6 contains the ratio of t/r_{ad}^6. Thus, the transfer events happening at earliest time will be dominated by the closest neighbors.

It is important to consider the sensitivity of the model to important inputs, in particular the radial distribution function $g(D)$ from eq 10 and volume fraction of the spheres in eqs 14 and 15. An excessive sensitivity with respect to these parameters will lead to model selection problems and limit the robustness of the sphere model as an analogy to nanostructuring. Figure 3 shows the expected observable for
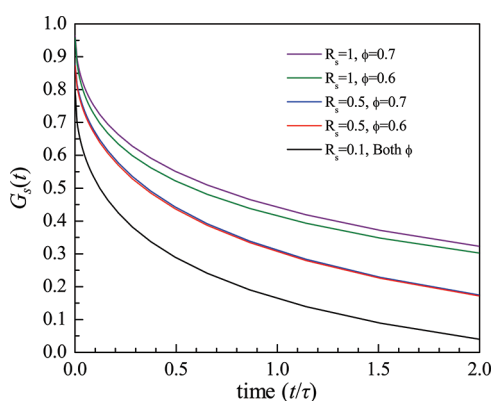

Figure 3. $\langle G_s(t) \rangle$ plotted for volume fractions $\varphi = 0.6$ and 0.7 for three R_s. Both black curves are for $R_s = 0.1$ and are identical. The red and blue curves are for $R_s = 0.5$ and are very similar. For $R_s = 1$ (green and purple curves), there is a difference, owing to the substantial contribution from spheres populated with multiple chromophores. For clarity, the pairs of curves at a particular R_s have been vertically offset.

two cases of sphere volume fractions, 0.6 and 0.7, at a bulk chromophore reduced concentration of $C = 1$. The sphere size is the reduced size; that is, it is divided by the Förster transfer

radius R_0. For small R_s (black curve), the curves are identical, consistent with the limits described above. The difference between the curves is still relatively minor at an intermediate size $R_s = 0.5$ (red and blue curves). For the sphere radius equal to the Förster radius, $R_s = 1$ (green and purple curves), the difference in the curves is significant. The chromophore used in the experiments, 9PA, has $R_0 = 19.7$ Å. For small spheres, therefore, the packing fraction does not significantly impact the fits. This is useful. For relatively small spheres, the volume fraction can be set to the calculated value. As discussed below, this turns out to be the situation that arises when fitting the experimental data.

A second input is the radial distribution function for the spheres. Two cases are calculated for a same sphere sizes as above, namely $R_s = 0.1$, 0.5, and 1. One uses an isotropic distribution of clusters, where $g(D)$ in eq 10 is constant and equal to 1 for all $D > R_s$. In this case, there is equal probability of finding two spheres with any separation greater than the distance required to prevent overlap. The second case uses the radial distribution function $g(D)$ for a hard sphere liquid at the same volume fraction of spheres, i.e., $\varphi = 0.7$.[51] A similar trend as that seen in Figure 3 is shown in Figure 4, with increasing, but modest, effect over the range of sphere sizes expected.
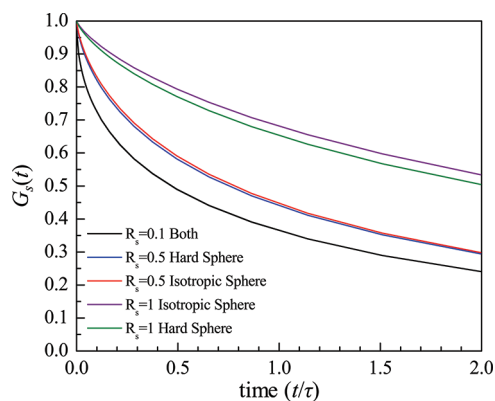

Figure 4. $\langle G_s(t) \rangle$ for different models of sphere radial distribution function. The pairs of curves are for $R_s = 0.1$, 0.5, and 1, calculated using $g(D)$ as either isotropic ($g(D) = 1$) or using the radial distribution function for a hard sphere liquid. The two curves at $R_s = 0.1$ cannot be differentiated.

These results demonstrate the robustness of using the sphere model to capture the essence of any nanostructuring when the characteristic radius is smaller than the Förster radius, R_0, that is $R_s < 1$. In this situation the number of parameters involved in analyzing the data is reduced. The experiments analyzed below fall into this situation. At larger scales, the volume fraction and form of radial distribution function become important and must be addressed. But because small R_s is the case for the relevant conditions that will occur in the following treatment, the radial distribution function can be set to 1 and the volume fraction to the calculated value of 0.7 without worrying about their effect on the results. By removing these parameters (volume fraction and radial distribution function) from consideration for moderate to small sphere sizes, only the size of the sphere remains as a source of difference in the excitation transfer. Any deviation in the excitation transfer from the expectation of the isotropic distribution of chromophores is therefore indicative of clustering. In addition, because the only sensitive parameter is

the sphere size, the length scale of clustering can be determined within experimental error.

B. Experimental Results. $\langle G_s(t) \rangle$ for 9PA is obtained by removing the rotational contribution from the fluorescence anisotropy via eq 12. The resulting curves are compared to the predictions from the chromophore distributions of the isotropic and clustered sphere models of excitation transfer. In Figure 5A,
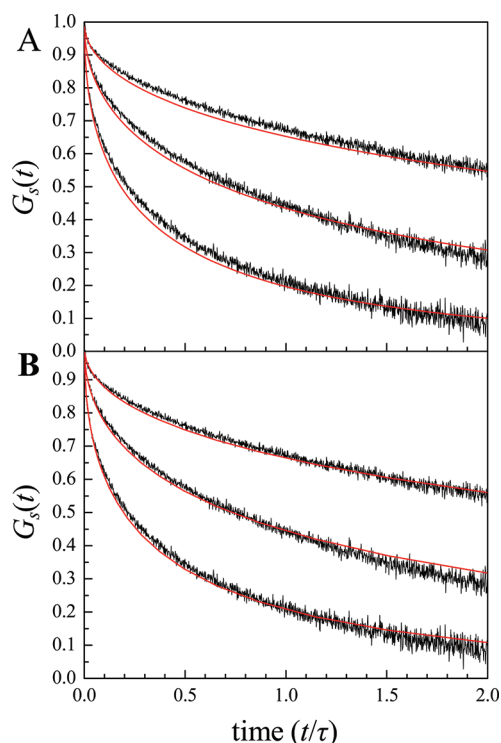

Figure 5. Global fits to the experimental data using the isotropic model. (A) Calculated curves use the experimental value $R_0 = 19.7$ Å. There are no adjustable parameters. The reduced concentrations, top curve to bottom curve are $C = 0.36$, 0.72, and 1.43. (B) R_0 is used as an adjustable parameter. The best fits are for $R_0 = 19.3$ Å. The reduced concentrations, top curve to bottom curve, are $C = 0.34$, 0.67, and 1.35.

the data are compared to the calculated curves using the isotropic model and the experimentally determined value of the Förster radius, $R_0 = 19.7$ Å. There are no adjustable parameters in the calculations. The agreement with the data for three concentrations is reasonable. The calculations reproduce the concentration dependence. The shapes of the curves are not perfect. There is reasonable agreement at early and late time, with noticeable deviations at intermediate times. Since these calculations use the isotropic model, they do not depend on a choice of radial distribution functions or volume fraction. The reasonable agreement with no adjustable parameters is an early indication that the size scale of any nanostructure cannot be large.

These calculations are sensitive to error in the experimentally determined Förster radius. To take into account possible error in R_0, the data are also fit using the isotropic model, but with R_0 used as an adjustable parameter. The fit is performed globally using weighted nonlinear least-squares. The variances for the experimental data are used as weighting factors. The results are shown in Figure 5B. By adjusting R_0 down from 19.7 to 19.3 Å, the fit is improved, decreasing the value of the reduced χ^2 from

3.0 to 1.5. Since there is some structure in the residuals, the confidence intervals for this fit were approximated using resampling of the residuals.[52] This is a bootstrap method that uses the residuals and fit parameters to create a synthetic data set to refit. Repetition builds up sufficient statistics to approximate the true distribution from which the estimates of R_0 are drawn. Using this approach, a 95% confidence interval for R_0 is constructed by ordering each estimate and finding the appropriate cutoffs from the list. For the isotropic model, this leads to a 95% confidence interval of [19.1 Å, 19.4 Å]. The interval is the fit bounds and does not take into account any other sources of systematic error or bias.

Figure 6 shows experimental data compared to the clustered sphere model using the experimentally determined value,
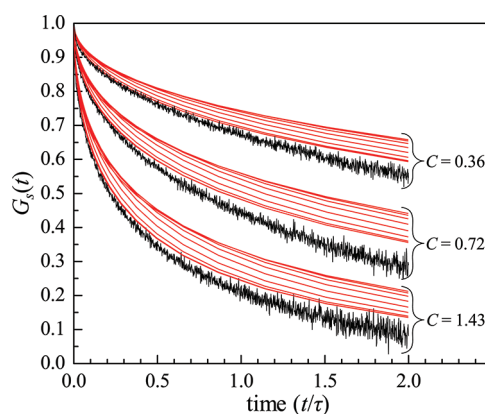

Figure 6. $\langle G_s(t) \rangle$ calculated with the clustered sphere model at the experimental value of $R_0 = 19.7$ Å. The black curves are the experimental data for each chromophore concentration as listed on the graph. The red curves are the clustered sphere calculations for $R_s = 0.1$, 0.2, 0.3, 0.4, 0.5, 0.6, 0.7, and 0.8 (lowest curve to top curve in each group, the same as in Figure 2). Because the value of R_0 is fixed, each calculated curve has no adjustable parameters.

$R_0 = 19.7$ Å. For each chromophore concentration, curves are generated for the clustered sphere model at various R_s from 0.1 to 0.9. Since R_0 and R_s are both fixed, there are no adjustable parameters for each curve shown; the curves are not fits to the data. In contrast to the case with the isotropic model calculations shown in Figure 5, there is very poor agreement between the experiment data and any of the clustered sphere calculations using $R_0 = 19.7$ Å. Since the excitation transfer only slows down with increasing sphere size, there is no reasonable value of R_s that can be chosen to fit the data using the $R_0 = 19.7$ Å (unless the spheres become unphysically large so the system is again isotropic).

In Figure 6, each curve is calculated with no adjustable parameters; the values of R_0 and R_s are fixed. Again because the valves of R_s are small (<1), it is not necessary to be concerned with a radial distribution function ($g(D) = 1$ is used), and the same calculated volume fraction of 0.7 is used for each curve. However, the calculations depend on both R_s and R_0, and there is experimental uncertainty in the determination of R_0. The data can be fit by varying both of these parameters. However, for clustered spheres, no simple regression can be performed because the model contains two parameters (R_0 and R_s), which are coupled when optimizing fits to $\langle G_s(t) \rangle$. Thus, there are a number of local minima, some of which are shown in Figure 7.
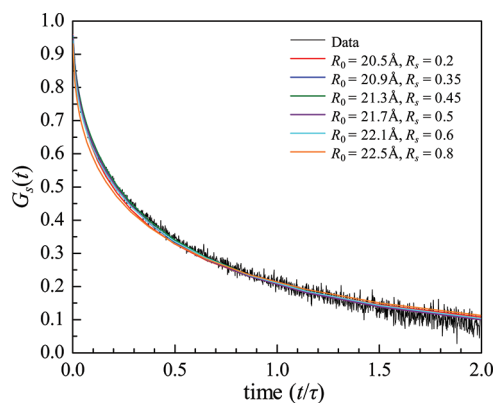
3060

dx.doi.org/10.1021/jp207757r | J. Phys. Chem. B 2012, 116, 3054–3064

Figure 7. Calculated $\langle G_s(t) \rangle$ for different pairs of $[R_0, R_s]$ that represent possible fits for the clustered sphere model. Only one concentration is shown for clarity, although the fits are global using all three concentrations' data. The curves are for $[R_0, R_s] = [20.5 \text{ Å}, 0.2]$, $[20.9 \text{ Å}, 0.35]$, $[21.3 \text{ Å}, 0.45]$, $[21.7 \text{ Å}, 0.5]$, $[22.1 \text{ Å}, 0.6]$, and $[22.5 \text{ Å}, 0.8]$. Other than the curve at $[22.5 \text{ Å}, 0.8]$ which fits poorly at early and late times, all other sets of parameter combinations perform about as well as the fits using the isotropic model.

C. Bayesian Analysis. In Figure 5A, the isotropic model does a reasonable job of describing the data with no adjustable parameters. In Figure 5B, it is shown that using one adjustable parameter, R_0, the agreement is improved. In Figure 7, it can be seen that the sphere calculations that represent nanostructuring can do a very good job of reproducing the data, but now there are two adjustable parameters, R_0 and R_s, and a range of pairs of these parameters can reproduce the data. It is necessary to decide between the models and the parameters. There is risk that the uncertainty in R_0 will cause a poor selection of parameters, even though for a particular set, the least-squares fit is better.

There is additional information, however, in that there is knowledge of what the Förster radius is within a range of values given by the error bars. Using Bayesian inference, this corresponds to prior knowledge of the distribution of parameters both models can take for the parameter R_0. With this information, model selection can be performed that fully incorporates the experimental data.

The Bayes factor formalism of model selection was developed by Jeffreys to perform scientific inference using the Bayes theorem.[53] For two models, both of which are equally likely candidates before the experiment, the Bayes factor represents the posterior odds of one model over the other, given the experimental data. This is represented as

$$B = \frac{\text{pr}(D|H_1)}{\text{pr}(D|H_0)} \tag{16}$$

with Bayes factor B, and $\text{pr}(D|H_i)$ as the probability of observing the data D, given the hypothesis H_i (known as the posterior odds). In this case, the index i takes two values: 0 for the null hypothesis of the isotropic model and 1 for the hypothesis of a clustered sphere model. The posterior probability is found by marginalizing the likelihood of the data given a hypothesis over all model parameters and their prior probabilities, as

$$\text{pr}(D|H_i) = \int \text{pr}(D|\theta_i, H_i)\pi(\theta_i|H_i)\, d\theta_i \tag{17}$$

The probability inside the integral is the likelihood of the data given the hypothesis parametrized by model parameters θ_i, and π is the prior probability for the model parameters. The value of the Bayes factor expresses the odds ratio of one hypothesis over another, corresponding to a weight of evidence.[54] Jeffreys provided a table of Bayes factors, and the level of support they correspond to in real situations. The table is heuristic but has endured owing to its repeated successful performance.[55] Table 1

Table 1. Strength of Evidence for Different Bayes Factors[55]

$\log_{10}(B)$	strength of evidence
0−0.5	not worth more than a mention
0.5−1.0	substantial
1.0−2.0	strong
>2.0	decisive

shows the base 10 logarithm of the Bayes factor and the strength of evidence for one hypothesis over another.

In this experiment, the two hypotheses are the isotropic model and the clustered sphere model. The Bayes factor therefore represents the strength of evidence for the clustered sphere model relative to the isotropic model. For the isotropic model, the only parameter is R_0. Its prior probability comes from the determination of its value and the associated error bars using spectroscopic observables. The error bar on the 19.7 Å value of R_0 is 0.7 Å. However, to increase the range in the Bayes analysis, we will take the prior distribution to be normally distributed, with a standard deviation of 1 Å.

$$\pi(R_0|H_{\text{iso}}) = \frac{1}{(2\pi\sigma_{R_0}{}^2)^{1/2}} \exp\left(-\frac{(R_0 - \hat{R}_0)^2}{2\sigma_{R_0}{}^2}\right) \tag{18}$$

The increase in the standard deviation used in the analysis reflects a desire to encompass unknown errors or biases that could be present. Comparing the shape of the curves for the isotropic and clustered sphere models at their maximum likelihood estimates, it is clear that the clustered sphere model is most benefitted from the relaxed width of the prior distribution. Thus, the broad prior distribution gives the clustered sphere model the best chances of fitting the data. The clustered sphere model contains two parameters, R_0 and R_s. The prior probability of the Förster radius is set identically for both models, as given in eq 18. For the sphere radius, a noninformative prior is chosen to reflect the fact that prior to the experiment; all values are equally likely up to a cutoff.

$$\pi(R_s|H_{\text{sph}}) = \frac{1}{R_{\text{max}}} \tag{19}$$

The cutoff radius is set at 22 Å. This value corresponds to the length of an OmimCl molecule with the octyl chain all-trans. For spheres larger than this, it would not be possible to pack OmimCl molecules in a manner that evokes the nanostructured picture of a hydrophobic pocket that the sphere model attempts to capture.

Using the above prior probabilities, Bayes factors were first computed for simulated data $\langle G_s(t) \rangle$ using both models at two values of R_0. Analysis of this simulated data will indicate the region over which the experiment is anticipated to be sufficiently sensitive to distinguish the two models. To simulate the data, theoretical curves calculated for $R_0 = 19.7$ Å and 19.3 Å were generated using the isotropic model, and the clustered

sphere model for R_s = 0.2 through 0.9 in 0.1 increments. These simulated data were then analyzed using the Bayes factors. Using the Bayes factors from the simulated data, it is possible to determine for which cases the experiment is able to distinguish the two models, and for which the uncertainty in R_0 makes distinguishing the models impossible. For example, since the calculate observable at very small R_s is very similar to the isotropic curve, it is anticipated that one would not be able to resolve these cases. This will be manifested by a small or possibly negative value of the Bayes factor B for that case of simulated data. Using the criteria in Table 1, it will be possible to determine for which cases a decision can be made, and for which no such determination is possible within the errors in this experiment. Because of the similarity between the two models that occurs at small R_s, the sensitivity will occur as a lower bound in R_s above which the two models can be distinguished via their Bayes factors.

The simulated data was assumed to have the experimentally measured variances, and the prior probability distributions were the same as will be used to analyze the experimental data. To compute the Bayes factors, eqs 16 and 17 were combined with the prior probabilities in eqs 18 and 19 and numerically integrated. For the likelihood function in eq 17, the data were assumed to be independent, normally distributed and heteroskedastic with variances taken to be those measured from the counting statistics in the fluorescence experiment. From the large number of points, the value of the integrand in eq 17 is highly peaked around the maximum likelihood estimate for the isotropic model, and a parametrized curve on R_0 and R_s in the clustered sphere model. The integration could therefore be performed using the Laplace approximation.[55] The integrand under this approximation for a model with d parameters becomes

$$I = (2\pi)^{d/2} |\tilde{\Sigma}|^{1/2} \mathrm{pr}(D|\tilde{\theta}, H)\pi(\tilde{\theta}, H) \qquad (20)$$

where all quantities are evaluated only at the estimator (denoted using $\sim$), and Σ is the negative inverse of the Hessian matrix on the log likelihood,

$$\Sigma = \{-\mathbf{D}^2 \log[\mathrm{pr}(D|\tilde{\theta}, H)\pi(\tilde{\theta}, H)]\}^{-1} \qquad (21)$$

The conditions under which the Laplace approximation can operate are normally taken to be that the number of data points $n > 20d$ (20 times the number of model parameters), which is well satisfied in this case.[55] Moreover, the structures of the predicted curves for both the isotropic and clustered sphere models are similar. Therefore, to a degree any errors are likely to be substantially offsetting when ratioed for the Bayes factor.

Table 2 gives the Bayes factors evaluated for simulated clustered sphere model data at two R_0s. Each cell represents a different set of conditions that was simulated, with the Bayes factor being how strongly one could accept the clustered sphere model over the isotropic model given the limitations of the experiment for that particular case. The trends are the same for both R_0s. For simulated data from very small spheres ($0 \leq R_s <$ 0.2), the Bayes factors are negative. This is a consequence of the Bayes factor's tendency to penalize overparameterized models that do not substantially improve the fit. Since the calculated curves for the lower limit of the clustered sphere model ($R_s < 0.2$) are almost identical to the isotropic model, the fits will be identical. But with more parameters, the clustered sphere model is selected against. At R_s = 0.3, the Bayes factor begins to rise into the realm of "substantial" based

Table 2. Bayes Factors for Support of the Clustered Sphere Model over the Isotropic Model at Different Simulated Conditions

	$\log_{10}(B)$	
sphere size	$R_0 = 19.3$ Å	$R_0 = 19.7$ Å
R_s = 0.0	−1.6	−1.7
R_s = 0.2	−0.85	−1.0
R_s = 0.3	0.61	0.50
R_s = 0.4	1.7	1.64
R_s = 0.5	1.4	1.23
R_s = 0.6	0.67	0.46
R_s = 0.7	0.70	0.54
R_s = 0.8	1.7	1.6
R_s = 0.9	3.1	3.1

on the Jeffreys criteria. The Bayes factors do not monotonically increase with increased sphere size but have a dip centered around R_s = 0.65. This results from coincidental improvement in the isotropic fit to the data as the component of $\langle G_s^{on}(t) \rangle$ in eq 5 begins to contribute. For smaller R_s at the occupation numbers relevant to the concentrations in this study, $\langle G_s^{on}(t) \rangle$ does not contribute due to the low probability of having two chromophores in a single small sphere. Even here, the evidence remains categorically "substantial." Further increase in the sphere size results in a rapid rise in the Bayes factor, reaching decisive levels for $R_s > 0.8$. These results show that the excitation transfer is sufficiently sensitive to detect the difference between an isotropic distribution of chromophores and the clustered distribution with $R_s > 0.3$. For smaller sized clusters, no evidence would be detected and the inference would likely call for rejecting the clustered hypothesis. This theoretical treatment includes the limitations from random experimental noise, since those experimentally relevant variances were used to compute the likelihoods.

Using the same computation method but with the experimental $\langle G_s(t) \rangle$ from the actual fluorescence data, the Bayes factor is calculated in the same manner as above. This will compare the isotropic model and clustered sphere against the experimental data. Because the Bayes factor analysis marginalizes on model parameters, it will not give optimal fit parameters. Instead, it will consider the two hypotheses as a whole when determining how strongly each model is supported by the experimental data. As the ratio is computed here, it represents whether the clustered sphere model can be accepted over the isotropic model. Because the experiment will only be sensitive for larger R_s, a negative result will be constrained by the upper limit of R_s over which the excitation transfer is anticipated to differentiate between the two models. The resulting Bayes factor calculated from the experimental data (expressed as $\log_{10}(B)$) has a value of 0.29. This puts it at the level of largely insignificant. The model selection indicates there is nothing in the experiment that strongly supports the clustered sphere model over the isotropic model for the distribution of 9PA in the ionic liquid. With regard to the picture of nanostructuring, this indicates that there is no appreciable structure on a length scale greater than $R_s \geq 0.3$, the range over which the experiment was shown to be able to distinguish the two models.

Using 19.7 Å for R_0, the results correspond to a lack of structure for radii of nanostructured domains of greater than 6 Å, which is the radius of the equivalent sphere used to describe the possible heterogeneity. In arriving at this value, it is important to check the previous assumptions about volume fraction

and sphere packing, as mentioned above. During the integration of eq 17 for the clustered sphere model using the experimental data, no maximum likelihood estimate contained an R_s greater than 0.65 that contribute to the integral. That is, while integrating along R_0, the likelihood for any point where the maximum likelihood has an $R_s > 0.65$ are so small as to be negligible. Therefore, all of the best fits correspond to the smaller values of R_s, in which reasonable changes in volume fraction or sphere packing negligibly impact the resulting calculated curve for $\langle G_s(t) \rangle$. Their influence can therefore safely be excluded from the calculations. Similarly, the broad prior probability distribution on the Förster radius gives the clustered sphere model the maximum chance of being accepted. Its rejection is therefore not the result of an overly hostile choice of the prior distribution. This conclusion is also resistant to proposed changes in the geometry of nanostructured domains. The key feature of the model is exclusion of probe molecules from a region of similar size to the Förster radius. This will be true of any nanostructured model of sufficiently large domains.

The upper bound of 6 Å puts the results of this experiment in line with other experiments,[15,16] which have tended to reduce the prominence of nanostructure organization in ionic liquids. Again referring to the previously computed van der Waals volumes as a rough guide of size, the 6 Å sphere would correspond to about 5 octyl chains combining to form the hydrophobic domain.

IV. CONCLUDING REMARKS

Donor−donor excitation transfer of 9-phenylanthracene dissolved in the room temperature ionic liquid 1-methyl-3-octylimidazolium chloride was measured at room temperature. Model calculations for the excitation transfer were computed for an unstructured solvent using an isotropic distribution of chromophores and a nanostructured solvent model using spheres to represent the hydrophobic domains. The spectroscopic observables were simulated, and it was shown that the excitation transfer experiments can differentiate the structured and unstructured models for sufficiently large nanostructured regions (sphere sizes). When compared to the time correlated fluorescence data for the 9-phenylanthracene in 1-methyl-3-octylimidazolium chloride, no evidence of large scale nanostructure is found.

The determination that there is no large scale structure is based on comparison of the donor−donor excitation transfer data at three different concentrations to two different models. It was found that an isotropic model does a reasonable job of reproducing the concentration dependent data with no adjustable parameters (Figure 5A). The concentration dependence is reproduced accurately and the shapes of the curves are reasonable. Improved agreement is found when the Förster radius, R_0, is allowed to vary within its error bars (Figure 5B). The isotropic model places the chromophores randomly. There is no nanostructuring.

When the model for the nanostructured liquid is used, which is based on a distribution of spheres to represent the nanostructured hydrophobic regions, it is apparently possible to improve the agreement between the calculations and the experimental data. The improvement is only possible using two adjustable parameters, the sphere size, R_s, (size of the hydrophobic domains) and R_0, rather than a single adjustable parameter for the isotropic model. However, applying Bayesian statistical methods, it was demonstrated that the probability is negligible, essentially zero, that the two parameter fits using the

theory of excitation transfer in the nanostructured model are meaningful. Tests using simulated data in model calculations and Bayesian statistics showed that if the system is nanostructured on a significant distance scale ($R_s > 0.3$), it would be apparent in the comparison between the data and the model calculations. For very small nanoscopic domains, the isotropic and nanostructured excitation transport models are indistinguishable. Therefore, the Bayesian analysis sets an upper bound on how large the nanostructured domains can be. On the basis of the experiments and the Bayesian analysis, the *upper bound* on the size of any nanostructured hydrophobic domains is a radius of 6 Å.

The results obtained here are consistent with recent neutron scattering experiments.[18] Aoun et al. discuss D_1, the repeat distance associated with the nanostructuring in a series of RTILs with different alkyl chain lengths. The longest chain length in this study is hexyl. The reported results show that each extra pair of carbons adds ~4.5 Å to the repeat distance. So 4.5 Å were added to the reported hexyl repeat distance to give a repeat distance for OmimCl of ~23 Å. The excitation transfer experiments and calculations presented here give a radius of organic region of ~6 Å. Then the diameter is ~12 Å. To obtain the ~23 Å repeat distance would require the diameter of the ionic regions to be ~11 Å, which is a reasonable result. Thus, the results of the excitation transfer study are in accord with the neutron scattering studies of Aoun et al.[20]

■ ASSOCIATED CONTENT

ⓢ Supporting Information
Segregation of 9-Phenylanthracene into the Alkyl Regions of OmimCl. This information is available free of charge via the Internet at http://pubs.acs.org.

■ AUTHOR INFORMATION

Corresponding Author
*E-mail: fayer@stanford.edu.

Notes
The authors declare no competing financial interest.

■ ACKNOWLEDGMENTS

■ REFERENCES

(1) Hu, Y.-F.; Liu, Z.-C.; Xu, C.-M.; Zhang, X.-M. *Chem. Soc. Rev.* **2011**, *40*, 3802−3823.
(2) Castner, E. W.; Margulis, C. J.; Maroncelli, M.; Wishart, J. F. *Annu. Rev. Phys. Chem.* **2011**, *62*, 85−105.
(3) Wishart, J. *J. Phys. Chem. Lett.* **2010**, *1*, 1629−1630.
(4) Hayes, R.; Warr, G. G.; Atkin, R. *Phys. Chem. Chem. Phys.* **2010**, *12*, 1709−1723.
(5) Wang, Y.; Voth, G. A. *J. Am. Chem. Soc.* **2005**, *127*, 12192−12193.
(6) Canongia Lopes, J. N. A.; Pádua, A. A. H. *J. Chem. Phys. B* **2006**, *110*, 3330−3335.
(7) Yanting, W.; Voth, G. A. *J. Phys. Chem. B* **2006**, *110*, 18601−18608.
(8) Mandal, P. K.; Sarkar, M.; Samanta, A. *J. Phys. Chem. A* **2004**, *108*, 9048−9053.
(9) Shigeto, S.; Hamaguchi, H.-o. *Chem. Phys. Lett.* **2006**, *427*, 329−332.

(10) Triolo, A.; Russina, O.; Bleif, H. J.; Cola, E. D. *J. Phys. Chem. B* **2007**, *111*, 4641−4644.

(11) Triolo, A.; Russina, O.; Fazio, B.; Appetecchi, G. B.; Carewska, M.; Passerini, S. *J. Chem. Phys.* **2009**, *130*, 164521−164526.

(12) Pott, T.; Meleard, P. *Phys. Chem. Chem. Phys.* **2009**, *11*, 5469−5475.

(13) Russina, O.; Triolo, A.; Gontrani, L.; Caminiti, R.; Xiao, D.; Hines, L. G.; Bartsch, R. A.; Quitevis, E. L.; Pleckhova, N.; Seddon, K. R. *J. Phys.-Con. Matt.* **2009**, *21*, 424121.

(14) Greaves, T. L.; Kennedy, D. F.; Mudie, S. T.; Drummond, C. J. *J. Phys. Chem. B* **2010**, *114*, 10022−10031.

(15) Hardacre, C.; Holbrey, J. D.; Mullan, C. L.; Youngs, T. G. A.; Bowron, D. T. *J. Chem. Phys.* **2010**, *133*, 074510.

(16) Annapureddy, H. V. R; Kashyap, H. K.; De Biase, P. M.; Margulis, C. J. *J. Chem. Phys. B* **2010**, *114*, 16838−16846.

(17) Russina, O.; Triolo, A. *Faraday Disc.* **2012**, *154*, 97−109.

(18) Russina, O.; Triolo, A.; Gontrani, L.; Caminiti, R. *J. Phys. Chem. Lett.* **2012**, *3*, 27−33.

(19) Wakasa, M.; Yago, T.; Hamasaki, A. *J. Chem. Phys. B* **2009**, *113*, 10559−10561.

(20) Aoun, B.; Goldbach, A.; Gonzalez, M. A.; Kohara, S.; Price, D. L.; Saboungi, M.-L. *J. Chem. Phys.* **2011**, *134*, 104509−104507.

(21) Fruchey, K.; Fayer, M. D. *J. Phys. Chem. B* **2010**, *114*, 2840−2845.

(22) Coleman, S.; Byrne, R.; Minkovska, S.; Diamond, D. *J. Chem. Phys. B* **2009**, *113*, 15589−15596.

(23) Xiao, D.; Hines, L. G.; Bartsch, R. A.; Quitevis, E. L. *J. Chem. Phys. B* **2009**, *113*, 4544−4548.

(24) Peterson, K. A.; Zimmt, M. B.; Linse, S.; Domingue, R. P.; Fayer, M. D. *Macromolecules* **1987**, *20*, 168−175.

(25) Ediger, M. D.; Domingue, R. P.; Fayer, M. D. *J. Chem. Phys.* **1984**, *80*, 1246−1253.

(26) Peterson, K. A.; Stein, A. D.; Fayer, M. D. *Macromolecules* **1990**, *23*, 111−120.

(27) Baumann, J.; Fayer, M. D. *J. Chem. Phys.* **1986**, *85*, 4087−4107.

(28) Gordon, G. W.; Berry, G.; Liang, X. H.; Levine, B.; Herman, B. *Biophys. J.* **1998**, *74*, 2702−2713.

(29) Schuler, B.; Lipman, E. A.; Eaton, W. A. *Nature* **2002**, *419*, 743−747.

(30) Gochanour, C. R.; Andersen, H. C.; Fayer, M. D. *J. Chem. Phys.* **1979**, *70*, 4254−4271.

(31) Gochanour, C. R.; Fayer, M. D. *J. Phys. Chem.* **1981**, *85*, 1989−1994.

(32) Ediger, M. D.; Fayer, M. D. *J. Phys. Chem.* **1984**, *88*, 6108−6116.

(33) Ediger, M. D.; Domingue, R. P.; Peterson, K. A.; Fayer, M. D. *Macromolecules* **1985**, *18*, 1182−1190.

(34) Klafter, J.; Blumen, A. *J. Lumin.* **1985**, *34*, 77−82.

(35) Huber, D. L. *Phys. Rev. B* **1979**, *20*, 2307−2314.

(36) Huber, D. L. *Phys. Rev. B* **1979**, *20*, 5333−5338.

(37) Peterson, K. A.; Fayer, M. D. *J. Chem. Phys.* **1986**, *85*, 4702−4711.

(38) Peterson, K. A.; Zimmt, M. B.; Linse, S.; Fayer, M. D. *ACS Symp. Ser.* **1987**, *358*, 323−342.

(39) Peterson, K. A.; Zimmt, M. B.; Fayer, M. D.; Jeng, Y. H.; Frank, C. W. *Macromolecules* **1989**, *22*, 874−879.

(40) Stein, A. D.; Peterson, K. A.; Fayer, M. D. *Chem. Phys. Lett.* **1989**, *161*, 16−22.

(41) Marcus, A. H.; Diachun, N. A.; Fayer, M. D. *J. Phys. Chem.* **1992**, *96*, 8930−8937.

(42) Hussey, D. M.; Keller, L.; Fayer, M. D. *Mol. Cryst. Liq. Cryst.* **1996**, *283*, 173−177.

(43) Marcus, A. H.; Fayer, M. D. *J. Chem. Phys.* **1991**, *94*, 5622−5630.

(44) Yang, P.; Voth, G. A.; Xiao, D.; Hines, L. G.; Bartsch, R. A.; Quitevis, E. L. *J. Chem. Phys.* **2011**, *135*, 034502.

(45) Forster, T. *Ann. Phys.* **1948**, *2*, 55−75.

(46) Ediger, M. D.; Fayer, M. D. *J. Chem. Phys.* **1983**, *78*, 2518−2524.

(47) Hemenger, R. P. a. P.; R., M. *J. Chem. Phys.* **1973**, *59*, 4064−4072.

(48) Bojarski, C.; Dudkiewicz, J. *Chem. Phys. Lett.* **1979**, *67*, 450−454.

(49) Singh, T. K., A. *J. Solution Chem.* **2009**, *38*, 1043−1053.

(50) Hamai, S.; Hirayama, F. *J. Phys. Chem.* **1983**, *87*, 83−89.

(51) de Haro, M. L.; Santos, A.; Yuste, S. B. *J. Chem. Phys.* **2006**, *124*, 236102.

(52) Carroll, R. J., Ruppert, D., Stefanski, L. A. *Measurement Error in Non-Linear Models*; CRC: Boca Raton, FL, 1995; Vol. 63.

(53) Jeffreys, H. *Proc. Cambridge Phil. Soc.* **1935**, *31*, 203−222.

(54) Good, I. J. *Weight of Evidence, a Brief Survey*; Elsevier: New York, 1985.

(55) Kass, R. E.; Raftery, A. E. *J. Am. Stat. Assoc.* **1995**, *90*, 773−795.